Stability of DIII-D high-performance, negative central shear discharges

J M Hanson[1], J W Berkery[1], J Bialek[1], M Clement[1,2], J R Ferron[3], A M Garofalo[3] C T Holcomb[4], R J La Haye[3], M J Lanctot[3], T C Luce[3], G A Navratil[1], K E J Olofsson[5], E J Strait[3], F Turco[1], A D Turnbull[3]

[1]Department of Applied Mathematics and Applied Physics, Columbia University, New York, New York 10027-6900, USA
[2]University of California San Diego, La Jolla CA 92093-0417, USA
[3]General Atomics, PO Box 85608, San Diego, California 92186-5608, USA
[4]Lawrence Livermore National Laboratory, 7000 East Ave, Livermore, California 94550, USA
[5]ORAU Oak Ridge Associated Universities, Oak Ridge, TN 37831, USA

Abstract. Tokamak plasma experiments on the DIII-D device [J. L. Luxon, *et al., Fusion Sci. and Tech.* **48** (2005) 807] demonstrate high-performance, negative central shear (NCS) equilibria with enhanced stability when the minimum safety factor $q_{\min}$ exceeds 2, qualitatively confirming theoretical predictions of favorable stability in the NCS regime. The discharges exhibit good confinement with an L-mode enhancement factor $H_{89} = 2.5$, and are ultimately limited by the ideal-wall external kink stability boundary as predicted by ideal MHD theory, as long as tearing mode (TM) locking events, resistive wall modes (RWMs), and internal kink modes are properly avoided or controlled. Although the discharges exhibit rotating TMs, locking events are avoided as long as a threshold minimum safety factor value $q_{\min} > 2$ is maintained. Fast timescale magnetic feedback control ameliorates RWM activity, expanding the stable operating space and allowing access to β_{N} values approaching the ideal-wall limit. Quickly growing and rotating instabilities consistent with internal kink mode dynamics are encountered when the ideal-wall limit is reached. The RWM events largely occur between the no- and ideal-wall pressure limits predicted by ideal MHD. However, evaluating kinetic contributions to the RWM dispersion relation results in a prediction of passive stability in this regime due to high plasma rotation. In addition, the ideal MHD stability analysis predicts that the ideal-wall limit can be further increased to $\beta_{\mathrm{N}} > 4$ by broadening the current profile. This path toward improved stability has the potential advantage of being compatible with the bootstrap-dominated equilibria envisioned for advanced tokamak (AT) fusion reactors.

PACS numbers: 52.25.Xz, 52.30.Cv, 52.35.Py, 52.55.fA, 52.55.Tn

Submitted to: *Nuclear Fusion*

1. Introduction

Fusion reactor design studies indicate that next-step devices based on the advanced tokamak (AT) concept will require a significant bootstrap current fraction $f_{\rm BS}$ in excess of 0.8 and normalized beta values near $\beta_{\rm N} \approx 5$ in order to meet performance goals [1, 2, 3]. Here, we define $\beta_{\rm N} = \beta/(I_{\rm p}/aB)$, with β the ratio of the plasma to magnetic field pressure (%), $I_{\rm p}$ the plasma current (MA), a the minor radius (m), and B the magnetic field (T). The combination of high $f_{\rm BS}$ and high $\beta_{\rm N}$ can potentially lead to unfavorable MHD stability. For example, the high bootstrap fraction is expected to result in a broad current density profile, and the $\beta_{\rm N}$ limit for ideal MHD stability typically scales with the normalized internal inductance $\ell_{\rm i}$ (a measure of the peakedness of the current density profile) in the absence of a perfectly conducting wall. Thus, the success of future AT devices will likely depend on maximizing passive MHD stability, through careful design of the equilibrium shape and profiles, and may require active stability control.

Theoretical calculations have identified profile characteristics expected to result in improved passive stability for bootstrap-dominated AT scenarios: (a) a safety factor profile $q(r) > 2$ everywhere eliminates resonances leading to poloidal and toroidal mode number $(m, n) = (2, 1)$ and $(3, 2)$ tearing mode (TM) instabilities, and (b) a region with negative magnetic shear $\mathrm{d}q/\mathrm{d}r$ near the plasma core makes the shear at the remaining higher order rational q-surfaces large except for in a small localized region [4, 5]. In addition, a core transport barrier is expected to result, leading to improved confinement. We will refer to this equilibrium paradigm as the negative central shear (NCS) configuration.

Some of the expected benefits of the NCS configuration have been confirmed experimentally. Early experiments in the DIII-D [6] and TFTR [7] tokamaks showed that predicted floor of neoclassical transport levels could be obtained in the NCS configuration. The DIII-D discharges accessed $3.5 < \beta_{\rm N} < 6$, but encountered $n = 1$ internal modes when the minimum safety factor $q_{\rm min}$ dropped below 2. In addition, NCS experiments have demonstrated high values of $f_{\rm BS}$ and equivalent fusion power [8, 9, 10], high poloidal beta $\beta_{\rm p}$ [11, 12], and quasistationary operation [13]. Subsequent DIII-D experiments transiently accessed a high confinement, high performance NCS regime characterized by an L-mode confinement enhancement factor $H_{89} = 2.5$, $\beta_{\rm N} = 4$, and $f_{\rm BS} > 0.6$ by ramping the toroidal field $B_{\rm t}$ to drive off-axis plasma current [14].

In the recent DIII-D experiments described here, we investigated the role of the current density profile in the stability of the previously established $B_{\rm t}$ ramp scenario, using off-axis neutral beam injection (NBI) to broaden the current and pressure profiles. We will describe the equilibrium formation technique and profiles in section 2, and example discharge waveforms, profiles, and cross-section shape are shown in figure 1 and figure 2. Off-axis NBI was previously used to demonstrate steady-state, high $q_{\rm min}$, monotonic shear discharges, with the finding that performance was limited by transport rather than stability [15]. In contrast, a key result from the new experiments is that

confinement is consistent with the previous B_t ramp data set, and performance is limited by the onset of long wavelength MHD instabilities that cause collapses of the plasma stored energy (i. e. β-collapses) and, in some cases, disruptions of the plasma current. We will describe the instabilities leading to β-collapses in more detail in section 3, and compare the conditions associated with the instability onsets with ideal MHD theory and modification by kinetic contributions [16], in section 4. Finally, we will discuss MHD stability optimization and control strategies in section 5.

2. Equilibrium formation technique

NCS discharges were created by inductively driving off-axis current using toroidal field ramps and by using off-axis NBI to further broaden the current density and pressure profiles. Waveforms from an example discharge are shown in figure 1. The toroidal field coil power supply voltage is brought to zero at time $t = 500$ ms, bringing about a ramp down of B_t with a decay time constant of 6.74 sec. NBI heating is applied early in the discharge, starting at $t = 50$ ms, to heat the plasma core and improve the efficiency of the B_t ramp current drive. Approximately 3.5 of the total 11 MW of NBI power is aimed 16.4 deg below the midplane (i. e. off-axis). The early heating brings about a transition to high-confinement mode (H-mode) at $t = 640$ ms, characterized by the emergence of pedestals in the edge electron temperature and density profiles and the onset of edge localized mode (ELM) activity. Approximately 1 MW of electron cyclotron (EC) power for current drive is applied at mid-radius. However, the EC current constitutes a small fraction of the total current during the high β_N phase due to the movement of the resonance location to the cold outer region of the plasma with the diminishing toroidal field.

Example equilibrium current density and pressure profiles are shown in figure 2. The B_t ramp inductively drives poloidal plasma current, resulting in a broad parallel current density profile [figure 2(a)] that is peaked at a normalized plasma minor radius of $\rho \approx 0.6$. Here, $\rho \equiv \sqrt{\phi/\phi(a)}$ with ϕ the toroidal magnetic flux. The fraction of parallel current driven by the B_t ramp is 0.22 at the time shown, $t = 1925$ ms. In contrast, the total beam driven current fraction is 0.17, with 0.056 from off-axis NBI, and the bootstrap current fraction is $f_{BS} = 0.37$. The B_t ramp current drive is obtained by calculating the electric field associated with the changing poloidal flux of the ramp, and evaluating Ohm's Law parallel to the equilibrium field using neoclassical resistivity as in Ref. [17]. The bootstrap and NBI contributions to the current are calculated using the TRANSP and NUBEAM codes [18, 19]. The total measured current density is obtained from equilibrium reconstructions constrained by motional stark effect (MSE) polarimetry [20], magnetic [21], and kinetic profile data.

The thermal contributions to the pressure profile p [figure 2(b)] are obtained from Thomson scattering measurements [22] of the electron temperature and density, and measurements of the carbon impurity temperature and density from charge exchange recombination (CER) spectroscopy [23]. The main (deuterium) ion density is inferred

from the electron and carbon density measurements using the known charge state of the carbon ions and assuming quasineutrality. The contribution to the pressure from fast neutral beam ions is simulated using NUBEAM. The pressure profile in figure 2(b) has a peaking factor $f_p \equiv p(0)/\langle p \rangle = 2.4$. Here, $\langle \cdot \rangle$ denotes a volume-average. The elevated pressure profile gradient in the region $0.5 < \rho < 0.6$ may consistent with an internal transport barrier (ITB). However, the more detailed transport analysis required to definitively prove the existence of an ITB is beyond the scope of the present work. The pressure peaking factors obtained during H-mode typically ranged from $2.4 \lessapprox f_p \lessapprox 3.4$, and this range is compatible with the previous DIII-D experiments where a definitive identification of ITB formation was made [14].

The increasing heating power and B_t ramp also bring about a steady increase in β_N. The β_N trajectory is interrupted by an ELM-free interval followed by a large ELM at $t = 1364$ ms, and again at $t = 2832$ ms by an internal kink mode. Nonetheless, an interval lasting approximately 400 ms with $\beta_\mathrm{N} \approx 4$ and $H_{89} \approx 2.5$ is obtained (shaded region in figure 1). For comparison, the energy confinement time during this interval is $\tau_\mathrm{E} \approx 120$ ms. In addition, f_BS reaches 0.6 during the high β_N interval. This performance is comparable to that obtained in previous DIII-D B_t ramp experiments [14].

Although the previous DIII-D B_t ramp experiments described in Ref. [14] were used as a starting point for the stability investigations described here, several important departures from the previous equilibrium formation technique that should be mentioned. First, off-axis NBI was used and the direction of the toroidal field was reversed in order to maximize the current drive from the off-axis beam [24]. The plasma shape was then altered to bias the divertor balance toward the lower divertor because $\vec{B}$ and therefore the ion $\vec{B} \times \nabla \vec{B}$ drift changed direction. In addition, the I_p evolution was adjusted to try to maintain $q_\mathrm{min} > 2$ for a longer time interval, and gas fueling was increased to try to shorten the ELM period. These changes may have affected fine details of the edge current profile, and therefore the global stability.

A final difference from the previous DIII-D experiments is that core EC heating was applied during the impurity burn-through phase (first 100 ms) on several discharges to investigate the impact of the early current profile on access to the high β_N phase. This technique has previously been shown to increase the early stored energy and reliability of the I_p ramp up in DIII-D ITER demonstration discharges [25]. We found that the application of EC heating in this early phase of the discharge allowed for a slower I_p ramp rate, resulted in less high frequency $n = 1$ MHD activity, and led to higher q_min compared with the ohmic only ramp up. However, the q_min evolution began to align well with that of the ohmic ramp up discharges after approximately 1500 ms, and little difference in the current profile was observed at the highest β_N values later in the discharge.

3. β-collapse and disruption precursor modes

It was found that the ultimate performance limits were determined by the onset of MHD instabilities rather than transport. All of the 26 discharges in the data set experienced at least one significant collapse of the plasma stored energy precipitated by an MHD instability. Furthermore, 4 of the 26 discharges suffered full disruptions of the plasma current within 100 ms or less of an MHD instability onset, and an additional 9 of the 26 discharges terminated in a disruption that was delayed more than 100 ms from the final β-collapse. The DIII-D plasma control system (PCS) was configured to initiate an early ramp down of the discharge if there were significant departures of I_p from the target or, in the final 13 discharges, if large poloidal magnetic field $\mathrm{d}B_\mathrm{p}/\mathrm{d}t$ fluctuations were detected. Early ramp downs were initiated in three shots when these tests failed, and it is possible that more disruptions could have been avoided with better tuning of the settings. However, the result that MHD stability determines the performance limit stands in contrast to the experience in DIII-D high q_min, off-axis NBI experiments with lower density, stationary B_t, and monotonic magnetic shear, where fast ion transport driven by Alfvén eigenmode activity limited the attainable normalized pressure to $\beta_\mathrm{N} \approx 3.5$ [15], motivating further analysis of the observed instabilities. Ideal MHD stability analysis of the previous monotonic shear discharges yielded a predicted ideal-wall limit of $4 \lessapprox \beta^\mathrm{iw}_\mathrm{N,lim} \lessapprox 5$ [15], suggesting that MHD stability may have posed a limitation if more heating power had been available.

Example timeseries from instabilities leading to β-collapses are shown in figure 3–figure 5. Cases where a rotating tearing mode (TM) locked preceded 29% of the collapses, and were characterized by a rotating precursor mode, usually with dominant poloidal and toroidal harmonics $(m, n) = (3, 1)$, that gradually slowed over several hundred ms (figure 3). The mode rotation frequency was consistent with the plasma ion rotation at the mode rational surface $q = m/n$ throughout the evolution to locking.

An additional 52% of the β-collapses were due to instabilities that were born locked or nearly locked in rotating plasmas, with mode rotation frequencies ranging from < 1 to 240 Hz (figure 4). The magnetic fluctuations of these born-locked modes had growth timescales of ≈ 1 ms, close to the DIII-D wall eddy current decay timescale τ_w. Although the modes lacked a coherent rotating precursor, they were preceded in many cases by intervals of damped magnetic response following ELM crashes. This behavior is consistent with close proximity to the resistive wall mode (RWM) marginal stability point, and edge-localized mode (ELM) crashes have previously been observed to drive RWMs in DIII-D [26, 27]. Although the majority of the RWM-driven collapses were due to $n = 1$ modes, two cases of dominantly $n = 2$ RWM activity were observed as well, during time intervals when the $n = 1$ RWM was controlled using magnetic feedback performed on a fast timescale comparable to τ_w (see section 5). In the example case shown in figure 4, the mode growth was observed during a time interval when slow time constant ($\tau = 50$ ms) magnetic feedback control of the perturbed n=1 field was applied. The slow feedback technique, sometimes referred to as "dynamic error field correction",

ameliorates the plasma response to any residual n=1 error field [28], thus making it unlikely that error field amplification is the cause of the unstable mode.

Furthermore, quickly rotating modes with growth timescales < 1 ms preceded 7% of the β-collapses. An example of such a quickly growing and rotating instability is shown in figure 5. The mode is born at a frequency consistent with the core plasma rotation, and rapidly chirps down in frequency. A > 40 G $n = 1$ excursion in the measured poloidal field occurs prior to the β-collapse, despite the use of $n = 1$ RWM feedback control. These dynamics are consistent with the evolution of an internal kink mode [29, 30], and the chirping behavior is also compatible with that of fast particle-driven off-axis fishbone modes observed in monotonic q discharges [31]. The poloidal dependence of the mode field measured at the DIII-D vessel wall was analyzed using a stochastic subspace identification technique [32], revealing a structure that is highly localized at the low field side midplane with a phase reversal on the high field side. This type of "phase-folded" structure is consistent with previous observations of internal MHD mode activity [33]. In addition, analysis with the GATO ideal MHD stability code [34] reveals an unstable $n = 1$ eigenmode that is strongly peaked in the region of zero shear near $\rho = 0.5$ with a small, but non-zero component in the vacuum region. The predicted mode remains unstable when an ideally conducting wall at the location of the DIII-D vacuum vessel is included in the GATO calculation.

Finally, 12% of the collapses were associated with large ELMs preceded by long (≈ 100 ms) ELM-free periods occurring early in the discharge following the H-mode transition. The occurrences of the TM locking, RWM, internal kink, and ELM β-collapse precursor modes are summarized in table 1.

4. MHD stability analysis

The stability of this group of NCS discharges is dependent on equilibrium characteristics (figure 6). For example, β-collapses due to RWM instabilities were primarily encountered when the approximate empirical ideal MHD no-wall limit scaling $\beta_{\mathrm{N,lim}}^{\mathrm{nw}} = 4\ell_{\mathrm{i}}$ [35] was approached and exceeded. (One RWM was driven by an ELM at low $\beta_{\mathrm{N}} = 1.2$ and $\ell_{\mathrm{i}} = 0.5$, outside the regime where the empirical no-wall limit scaling law is expected to apply [35].) On the other hand, cases of rotating TMs that lock are largely independent of β_{N}, but only occur when $q_{\mathrm{min}} < 2$. Finally, incidences of internal kink mode onset occur when $q_{\mathrm{min}} \approx 2$, consistent with observations from previous NCS experiments on DIII-D and JT-60U [6, 8]. The complete parameter space covered by the experiment (grey lozenges in figure 6) was obtained by time-averaging β_{N}, ℓ_{i}, and q_{min} waveforms from all discharges over 50 ms intervals.

4.1. Ideal MHD β_{N}-limits

The β_{N} limits predicted by ideal MHD theory are consistent with the observed stability. The ℓ_{i} and q_{min} dependencies of the limits shown in figure 6 were evaluated systematically

by scaling the current density profile of an experimental equilibrium by a factor $1 + \alpha(\psi - 0.5)$ with ψ the normalized poloidal flux and $-0.5 < \alpha < 0.5$. The original and scaled parallel current density and safety factor profiles are shown in figure 7. The β_N limits were then calculated by scaling the equilibrium pressure until a sign change was identified in the perturbed potential energy δW predicted by the DCON code [36], for cases without (nw) and with (iw) an ideally conducting wall in the calculation.

It is important to emphasize that the stability analysis is based on a scaled family of equilibria that are derived from a single experimental equilibrium. This technique has the advantage of producing a smooth series of curves representing the stability limits in parameter space. However, the scaled profiles from the study may not be exactly consistent with experimental equilibria that have matching integral properties, such as β_N and ℓ_i. Nonetheless, the predicted stability limits of the scaled equilibria are compatible with the β-collapse data set. The majority of the collapses due to RWM events are above the predicted no-wall limit, and the predicted ideal-wall limit is consistent with the highest accessed β_N values. In two cases, internal kink modes were encountered at the predicted ideal-wall limit when the RWM was stabilized using magnetic feedback.

In addition, a weakening of the stability is predicted by the scaling study as q_{min} drops below 2, coincident with a drop in the critical β_N value for RWM events. This strong sensitivity of the stability to the existence of an internal $q = 2$ surface is consistent with previous theoretical investigations of the critical wall position for stabilizing external kink modes in DIII-D NCS equilibria [37].

4.2. Kinetic contributions to RWM stability

Resistive wall mode activity contributed to the largest fraction of β-collapses described in section 3 and appears to be largely bounded by the no-wall and ideal-wall β_N limits predicted by ideal MHD theory. An additional question remains as to whether the theory of kinetic modifications to ideal MHD stability [16] can yield a more precise understanding of the marginal stability point.

Neglecting the perturbed kinetic energy δK, the dispersion relation for the low-frequency (i. e. sub-Alfvénic) RWM growth rate γ and rotation rate ω can be written as

$$(\gamma + i\omega)\tau_w = -\frac{\delta W_{nw} + \delta W_k}{\delta W_{iw} + \delta W_k}, \tag{1}$$

where τ_w is the characteristic wall eddy current decay timescale and δW_k represents the kinetic contributions to the perturbed potential energy [16]. Equation (1) is valid when ideal MHD predicts an instability without a wall ($\delta W_{nw} < 0$) that can be stabilized by the presence of an ideally conducting wall ($\delta W_{iw} > 0$), and it has been successful in explaining the onsets of unstable RWMs in NSTX [38] and the damping rate of the driven, stable RWM in several devices [39, 40, 41, 42]. DIII-D and JT-60U experiments have demonstrated passively stable operation in rotating discharges with $\delta W_{nw} < 0$, and

the stability has been attributed to the rotational stabilization of the RWM [43, 44, 45]. The kinetic dispersion relation can be understood to include the stabilizing influence of a torque between a rotating plasma and the RWM [46], and thus can presumably explain the observed DIII-D and JT-60U cases of passive RWM stability.

Key stabilizing contributions to $\delta W_{\rm k}$ include the influences of plasma collisionality, fast ion motion, and resonances between the plasma $E \times B$ rotation $\omega_{\rm E}$ and the trapped ion precession drift frequency $\omega_{\rm D}$ and bounce frequency harmonics $l\omega_{\rm b}$ [38, 47]. The evolution of the $\omega_{\rm E}$ profile for a discharge with RWM feedback control is shown in figure 8. This discharge reaches the ideal-wall $\beta_{\rm N}$ limit at approximately $t = 2600$ ms and suffers a β-collapse due to an internal kink mode shortly thereafter. Example $\omega_{\rm E}$, $\omega_{\rm b}$, $\omega_{\rm D}$ and electron–ion collision frequency profiles for this discharge and a lower $\beta_{\rm N}$ companion case without RWM feedback are shown in figure 9. In both cases, $\omega_{\rm E}$ is comparable in magnitude to $\omega_{\rm b}$ at mid-radius, and the resonance between $\omega_{\rm E}$ and harmonics of $\omega_{\rm b}$ is primarily responsible for the kinetic stabilization. The profiles in figure 9 can be contrasted with those in Ref. [40], wherein $\omega_{\rm E}$ was swept through the $\omega_{\rm b}$ and $\omega_{\rm D}$ resonances.

The kinetic effects are sufficient to yield a prediction of RWM stability even near the ideal MHD ideal-wall limit $\beta_{\rm N,lim}^{\rm iw}$. Solutions for the RWM growth rate γ obtained using the MISK code [38] are shown in figure 8(c). The code uses a perturbative approach for solving (1) in which γ and ω terms are omitted from the expression for $\delta W_{\rm k}$. In addition, the stabilizing contributions from fast ions were neglected. The ideal MHD and kinetic calculations of γ are not shown for $t > 2650$ ms because the the ideal MHD stability calculation predicts that the discharges becomes unstable with a wall ($\delta W_{\rm iw} < 0$) after this time, and therefore the RWM dispersion relation given in (1) is no longer valid. Because of the strong plasma rotation, the kinetic contributions arise mainly from the resonances between $\omega_{\rm E}$ and harmonics of $\omega_{\rm b}$.

Proximity to the marginal stability point was assessed by artificially scaling the $\omega_{\rm E}$ profiles for the two experimental cases in figure 9. The growth rate from the scaling study is shown as a function of the scaled value of $\omega_{\rm E}$ at the magnetic axis in figure 10. The lower $\beta_{\rm N}$ case reaches the marginal point when the $\omega_{\rm E}$ rotation on axis reaches 43 krad/s, corresponding to a 72% reduction in the rotation profile, indicating that a large change is needed in the experimental rotation to reach the marginal point.

The MISK simulations predict that the kinetic effects exert a strong stabilizing influence throughout the wall-stabilized regime. Figure 11 shows the ideal MHD and kinetic contributions to the perturbed energy and growth rates as a function of $c_\beta \equiv (\beta_{\rm N} - \beta_{\rm N,lim}^{\rm nw})/(\beta_{\rm N,lim}^{\rm iw} - \beta_{\rm N,lim}^{\rm nw})$. The calculations are based on experimental equilibria and kinetic profiles for four different cases with $1.9 < q_{\rm min} < 2.1$. The ideal MHD δW terms decrease with c_β, leading to a strong increase in the ideal MHD growth rate. However, in these cases, the kinetic effects are sufficient to confer stability across the entire range of c_β values.

5. MHD stability optimization and control

The dependencies of the precursor modes leading to β-collapses shown in figure 6 indicate that many of the collapses can be avoided through careful choice of the current density profile. Specifically, collapses due to TM locking and internal kink events are avoided when $q_{\min} > 2$, and a reduction in the critical β_N for RWM events and a weakening of the predicted ideal MHD stability are observed when $q_{\min}$ crosses 2 from above. This overall weakening of the stability is likely related to the introduction of a low order rational surface $q = m/n = 2$ in a region of zero magnetic shear. If the collapses due to TM locking and internal kink modes can be passively avoided, the final remaining instability is the RWM.

Fortunately, the RWM is amenable to control with magnetic feedback [48, 49]. In what has now become a standard approach for DIII-D, fast timescale $n = 1$ magnetic RWM control was applied in the NCS experiments using a proportional gain feedback algorithm incorporating the internal non-axisymmetric coils (I-coils) and internal B_p sensors on the low field side midplane [figure 2(c)]. In addition, a feedforward, quasi-dc correction for the known DIII-D intrinsic error field was superposed with the I-coil feedback commands. This approach facilitated access to a regime of high β_N values close to the predicted ideal-wall limit (figure 12). (Similar to figure 6, the data points shown in figure 12 were obtained by time-averaging waveforms from all discharges over 50 ms intervals. The slower timescale, "dynamic error correction" feedback case referred to in the discussion of figure 4 in section 3 is not counted as RWM feedback in figure 12, since this slowed feedback would not be expected to suppress an unstable RWM.) However, RWM instabilities were not fully eliminated for the following reasons: (a) some RWMs occurred early in the discharges, before active feedback was enabled; (b) in several instances RWM instabilities grew despite the use of feedback; and (c) RWMs that occurred during feedback sometimes caused the feedback power supplies to exceed their current limits and trip off, allowing the growth of an additional RWM following a recovery to a high β_N state later in the discharge. In the cases where an RWM occurred during feedback, there were two instances of $n = 2$ mode growth that could not be controlled by the $n = 1$ feedback scheme, and 5 cases where the mode grew quickly enough to bring the power supplies to their limits. Thus, it may be possible to further ameliorate the RWM-induced β-collapses by extending the feedback control to $n > 1$ and by improving robustness, for example by using a state-space control algorithm [50, 51].

6. Conclusions

DIII-D experiments have uncovered a class of elevated $q_{\min}$, NCS equilibria that exhibit favorable performance and confinement ($\beta_N = 4$, $H_{89} = 2.5$) and access the ideal-wall β_N limit predicted by ideal MHD theory. The onset of TM locking, RWM, and internal kink instabilities determines performance limits, but these modes can largely be either avoided, through optimization of the current profile, or controlled. Specifically, collapses

of the plasma stored energy due to TM locking events and the onset of internal kink modes are avoided if $q_{\min}$ remains greater than 2 and β_{N} remains below the predicted ideal-wall limit.

In addition, collapses due to RWMs are ameliorated using magnetic feedback control, although the control fails in some instances, indicating the need for improved robustness. The observed instability onsets are compatible with the predictions of ideal MHD theory, inasmuch as a weakening of the stability is predicted when $q_{\min}$ crosses 2 from above, and as most of the RWM events occur at β_{N} values between the predicted no-wall and ideal-wall limits. Thus, the optimization of passive stability and the improvement of active instability control are paramount for improving the performance of NCS discharges.

Although the onsets of RWM events are largely bounded by the no-wall and ideal-wall β_{N} limits predicted by ideal MHD, calculations that incorporate kinetic contributions to the ideal theory predict stability for some cases across this regime. The kinetic stabilization is mainly attributed to a resonance between the plasma ω_{E} rotation and the bounce frequency of trapped ions ω_{b}. The simulation results appear to be at odds with the interpretation of this class of β-collapse precursors as RWMs, and with the demonstrated benefit of RWM feedback in facilitating access to the ideal-wall limit. One possible explanation for the apparent contradiction is that the equilibrium and profile analysis, conducted at 40 ms intervals based on the availability of MSE data, does not have sufficient time-resolution to capture profile fluctuations that transiently violate the marginal stability threshold. This shortcoming could be addressed by more careful programming of the neutral beam waveforms needed for the MSE and CER profile measurements prior to RWM events, and active MHD spectroscopy may also prove useful in measuring the stable RWM damping rate for quantitative comparisons with the kinetic theory, as in Refs. [39], [40], and [41]. In addition, it is likely the case that using RWM feedback helps improve the passive stability by quickly damping the plasma response to transient events such as ELMs as in Ref. [44], thereby minimizing rotation braking associated with the response. A third possible explanation is that additional physics is needed in the simulations. For example, recent comparisons of current-driven kink mode simulations with experimental mode onsets have uncovered the need to include resistive effects [52].

The maximum ideal-wall limit, $\beta_{\mathrm{N,lim}}^{\mathrm{iw}} \approx 4.5$, yielded by ideal MHD simulations of the scaled current profile equilibria is significantly lower than the ideal-wall limit uncovered in previous studies of similar DIII-D discharges, $5 \lessapprox \beta_{\mathrm{N,lim}}^{\mathrm{iw}} \lessapprox 6$ [14]. A possible reason for this discrepancy is that there are some minor differences in the discharge programming from the previous experiments, including the I_{p} waveform and gas fuelling, described in more detail in section 2. It may be that these differences affected the edge current profile gradients, and thereby the global MHD stability. More careful comparisons between the new and previous experimental equilibria may help resolve this discrepancy and yield important insights into the optimization of passive MHD stability.

This work does not independently address the impact of pressure profile shape effects, such as a the formation of ITBs, for stability. The data set of MHD-driven β-collapses obtained does not exhibit a strong sensitivity to the pressure peaking factor f_p, and we note that a correlation between f_p and ℓ_i has been previously observed in high-β_N, high-q_{min} DIII-D discharges [53]. However, the influence of pressure profile shape is included in the MHD simulations with which this data set was compared, and has previously been investigated in the study of a larger NSTX data set and in simulations of ITER steady-state discharges [54, 55].

In addition to demonstrating the importance of maintaining $q_{min} > 2$, ideal MHD stability analysis of scaled current profile equilibria indicates that the ideal-wall limit begins to exceed the experimentally accessed β_N values as ℓ_i is decreased (figure 6). It is worth pointing out that the no-wall limit predicted by the scaling study exhibits the opposite trend, that is, it increases as ℓ_i increases. However, the success of RWM feedback in facilitating access to the ideal-wall limit makes *it* the limit of primary concern. The high ideal-wall limit regime with elevated $q_{min} > 2$ and low $\ell_i < 0.65$ was not explored at high β_N because the discharges naturally evolved toward lower q_{min} and higher ℓ_i as the heating power was increased (figure 6). Heating and current drive upgrades, such as increasing the amount of available off-axis NBI power, may help to sustain a low-ℓ_i, high-q_{min}, NCS current profile at high β_N in steady-state. This path toward improved stability has the potential advantage of being compatible with the broad current profile, bootstrap-dominated equilibria envisioned for advanced tokamak fusion reactors.

Acknowledgments

This work was supported in part by the U. S. Department of Energy under DE-FG02-04ER54761, DE-FG02-99ER54524, DE-FG02-07ER54917, DE-FC02-04ER54698, DE-AC52-07NA27344, and DE-FG02-95ER54309. DIII-D data shown in this paper can be obtained in digital format by following the links at `https://fusion.gat.com/global/D3D_DMP`.

References

[1] Najmabadi F, Abdou A, Bromberg L, Brown T, Chan V, Chu M, Dahlgren F, El-Guebaly L, Heitzenroeder P, Henderson D, John H S, Kessel C, Lao L, Longhurst G, Malang S, Mau T, Merrill B, Miller R, Mogahed E, Moore R, Petrie T, Petti D, Politzer P, Raffray A, Steiner D, Sviatoslavsky I, Synder P, Syaebler G, Turnbull A, Tillack M, Waganer L, Wang X, West P and Wilson P 2006 *Fusion Engineering and Design* **80** 3 – 23 ISSN 0920-3796 <ce:title>Aries - AT Special Issue</ce:title>

[2] Chan V, Stambaugh R, Garofalo A, Canik J, Kinsey J, Park J, Peng M, Petrie T, Porkolab M, Prater R, Sawan M, Smith J, Snyder P, Stangeby P and Wong C 2011 *Nuclear Fusion* **51** 083019

[3] Kessel C E, Tillack M S, Najmabadi F, Poli F M, Ghantous K, Gorelenkov N, Wang X R, Navaei D, Toudeshki H H, Koehly C, EL-Guebaly L, Blanchard J P, Martin C J, Mynsburge L, Humrickhouse P, Rensink M E, Rognlien T D, Yoda M, Abdel-Khalik S I, Hageman M D, Mills

B H, Rader J D, Sadowski D L, Snyder P B, St John H, Turnbull A D, Waganer L M, Malang S and Rowcliffe A F 2015 *Fusion Science and Technology* **67** 1

[4] Kessel C, Manickam J, Rewoldt G and Tang W M 1994 *Phys. Rev. Lett.* **72** 1212–1215

[5] Turnbull A D, Taylor T S, Lin-Liu Y R and John H S 1995 *Phys. Rev. Lett.* **74** 718–721

[6] Strait E J, Lao L L, Mauel M E, Rice B W, Taylor T S, Burrell K H, Chu M S, Lazarus E A, Osborne T H, Thompson S J and Turnbull A D 1995 *Phys. Rev. Lett.* **75**(24) 4421–4424

[7] Levinton F M, Zarnstorff M C, Batha S H, Bell M, Bell R E, Budny R V, Bush C, Chang Z, Fredrickson E, Janos A, Manickam J, Ramsey A, Sabbagh S A, Schmidt G L, Synakowski E J and Taylor G 1995 *Phys. Rev. Lett.* **75**(24) 4417–4420

[8] Fujita T, Kamada Y, Ishida S, Neyatani Y, Oikawa T, Ide S, Takeji S, Koide Y, Isayama A, Fukuda T, Hatae T, Ishii Y, Ozeki T, Shirai H and JT-60 Team 1999 *Nuclear Fusion* **39** 1627

[9] Fujita T, Ide S, Kamada Y, Suzuki T, Oikawa T, Takeji S, Sakamoto Y, Koide Y, Isayama A, Hatae T, Kubo H, Higashijima S, Naito O, Shirai H and Fukuda T 2001 *Phys. Rev. Lett.* **87**(8) 085001

[10] Lazarus E A, Navratil G A, Greenfield C M, Strait E J, Austin M E, Burrell K H, Casper T A, Baker D R, DeBoo J C, Doyle E J, Durst R, Ferron J R, Forest C B, Gohil P, Groebner R J, Heidbrink W W, Hong R M, Houlberg W A, Howald A W, Hsieh C L, Hyatt A W, Jackson G L, Kim J, Lao L L, Lasnier C J, Leonard A W and Lohr J 1996 *Phys. Rev. Lett.* **77** 2714–2717

[11] Politzer P A, Casper T, Forest C B, Gohil P, Heidbrink W W, Hyatt A W, James R A, Jong R, Lao L L, Makowski M, Meyer W, Porter G D, Sager G T, Stallard B W, St John H, Thompson S J, Turnbull A D and Wròblewski D 1994 *Physics of Plasmas (1994-present)* **1** 1545–1553

[12] Hobirk J, Wolf R C, Gruber O, Gude A, Günter S, Kurzan B, Maraschek M, McCarthy P J, Meister H, Peeters A G, Pereverzev G V, Stober J, Treutterer W and ASDEX Upgrade Team 2001 *Phys. Rev. Lett.* **87**(8) 085002

[13] Crisanti F, Litaudon X, Mailloux J, Mazon D, Barbato E, Baranov Y, Bécoulet A, Bécoulet M, Challis C D, Conway G D, Dux R, Eriksson L G, Esposito B, Frigione D, Hennequin P, Giroud C, Hawkes N, Huysmans G, Imbeaux F, Joffrin E, Lomas P, Lotte P, Maget P, Mantsinen M, Moreau D, Rimini F, Riva M, Sarazin Y, Tresset G, Tuccillo A A and Zastrow K D 2002 *Phys. Rev. Lett.* **88**(14) 145004

[14] Garofalo A M, Doyle E J, Ferron J R, Greenfield C M, Groebner R J, Hyatt A W, Jackson G L, Jayakumar R J, Kinsey J E, La Haye R J, McKee G R, Murakami M, Okabayashi M, Osborne T H, Petty C C, Politzer P A, Reimerdes H, Scoville J T, Solomon W M, John H E S, Strait E J, Turnbull A D, Wade M R and VanZeeland M A 2006 *Physics of Plasmas* **13** 056110 (pages 10)

[15] Holcomb C, Ferron J, Luce T, Petrie T, Park J, Turco F, Zeeland M V, Okabayashi M, Lasnier C, Hanson J, Politzter P, In Y, Hyatt A, Haye R L and Lanctot M 2014 *Nuclear Fusion* **54** 093009

[16] Hu B and Betti R 2004 *Phys. Rev. Lett.* **93** 105002

[17] Forest C B, Kupfer K, Luce T C, Politzer P A, Lao L L, Wade M R, Whyte D G and Wròblewski D 1994 *Phys. Rev. Lett.* **73**(18) 2444

[18] Hawryluk R J 1979 An empirical approach to tokamak transport *Course on Physics of Plasma Close to Thermonuclear Conditions* (Varenna, Italy)

[19] Pankin A, McCune D, Andre R, Bateman G and Kritz A 2004 *Computer Physics Communications* **159** 157 – 184 ISSN 0010-4655

[20] Holcomb C T, Makowski M A, Jayakumar R J, Allen S A, Ellis R M, Geer R, Behne D, Morris K L, Seppala L G and Moller J M 2006 *Review of Scientific Instruments* **77** 10E506 (pages 3)

[21] Strait E J 2006 *Review of Scientific Instruments* **77** 023502 (pages 14)

[22] Carlstrom T N, Campbell G L, DeBoo J C, Evanko R, Evans J, Greenfield C M, Haskovec J, Hsieh C L, McKee E, Snider R T, Stockdale R, Trost P K and Thomas M P 1992 *Review of Scientific Instruments* **63** 4901–4906

[23] Burrell K H, Kaplan D H, Gohil P, Nilson D G, Groebner R J and Thomas D M 2001 *Review of Scientific Instruments* **72** 1028–1033

[24] Murakami M, Park J, Petty C, Luce T, Heidbrink W, Osborne T, Prater R, Wade M, Anderson

P, Austin M, Brooks N, Budny R, Challis C, DeBoo J, deGrassie J, Ferron J, Gohil P, Hobirk J, Holcomb C, Hollmann E, Hong R, Hyatt A, Lohr J, Lanctot M, Makowski M, McCune D, Politzer P, Scoville J, John H S, Suzuki T, Taylor T, West W, Unterberg E, Zeeland M V and Yu J 2009 *Nuclear Fusion* **49** 065031 (8pp)

[25] Jackson G, Casper T, Luce T, Humphreys D, Ferron J, Hyatt A, Lazarus E, Moyer R, Petrie T, Rudakov D and West W 2008 *Nuclear Fusion* **48** 125002

[26] Reimerdes H, Garofalo A M, Okabayashi M, Strait E J, Betti R, Chu M S, Hu B, In Y, Jackson G L, La Haye R J, Lanctot M J, Liu Y Q, Navratil G A, Solomon W M, Takahashi H, Groebner R J and the DIII-D team 2007 *Plasma Physics and Controlled Fusion* **49** B349–B358

[27] Okabayashi M, Bogatu I, Chance M, Chu M, Garofalo A, In Y, Jackson G, La Haye R, Lanctot M, Manickam J, Marrelli L, Martin P, Navratil G, Reimerdes H, Strait E, Takahashi H, Welander A, Bolzonella T, Budny R, Kim J, Hatcher R, Liu Y and Luce T 2009 *Nuclear Fusion* **49** 125003 (16pp)

[28] Garofalo A, La Haye R and Scoville J 2002 *Nuclear Fusion* **42** 1335–1339

[29] Lao L L, Burrell K H, Casper T S, Chan V S, Chu M S, DeBoo J C, Doyle E J, Durst R D, Forest C B, Greenfield C M, Groebner R J, Hinton F L, Kawano Y, Lazarus E A, Lin-Liu Y R, Mauel M E, Meyer W H, Miller R L and Navratil G A 1996 *Physics of Plasmas* **3** 1951 ISSN 1070664X

[30] Callen J D, Hegna C C, Rice B W, Strait E J and Turnbull A D 1999 *Physics of Plasmas* **6** 2963–2967

[31] Okabayashi M, Matsunaga G, deGrassie J S, Heidbrink W W, In Y, Liu Y Q, Reimerdes H, Solomon W M, Strait E J, Takechi M, Asakura N, Budny R V, Jackson G L, Hanson J M, La Haye R J, Lanctot M J, Manickam J, Shinohara K and Zhu Y B 2011 *Physics of Plasmas* **18** 056112 ISSN 1070664X

[32] Olofsson K E J, Hanson J M, Shiraki D, Volpe F A, Humphreys D A, La Haye R J, Lanctot M J, Strait E J, Welander A S, Kolemen E and Okabayashi M 2014 *Plasma Physics and Controlled Fusion* **56** 095012

[33] Kim J S, Chance M S, Edgell D H, Greene J M, Strait E J and Turnbull A D 2001 *Plasma Physics and Controlled Fusion* **43** 1593

[34] Bernard L C, Helton F J and Moore R W 1981 *Computer Physics Communications* **24** 377 – 380 ISSN 0010-4655

[35] Strait E J 1994 *Physics of Plasmas* **1** 1415–1431

[36] Glasser A H 2016 *Physics of Plasmas* **23** 072505

[37] Lee B, Turnbull A and Taylor T 1997 *Nuclear Fusion* **37** 1271

[38] Berkery J W, Sabbagh S A, Reimerdes H, Betti R, Hu B, Bell R E, Gerhardt S P, Manickam J and Podestà M 2010 *Physics of Plasmas* **17** 082504 (pages 11)

[39] Chapman I T, Gryaznevich M P, Howell D F, Liu Y Q and the MAST Team 2011 *Plasma Physics and Controlled Fusion* **53** 065022

[40] Reimerdes H, Berkery J W, Lanctot M J, Garofalo A M, Hanson J M, In Y, Okabayashi M, Sabbagh S A and Strait E J 2011 *Phys. Rev. Lett.* **106** 215002

[41] Berkery J W, Sabbagh S A, Balbaky A, Bell R E, Betti R, Diallo A, Gerhardt S P, LeBlanc B P, Manickam J, Menard J E and Podestà M 2014 *Physics of Plasmas (1994-present)* **21** 056112

[42] Turco F, Turnbull A D, Hanson J M and Navratil G A 2015 *Physics of Plasmas* **22** 022503

[43] Strait E J, Taylor T S, Turnbull A D, Ferron J R, Lao L L, Rice B, Sauter O and Thompson S J 1995 *Physical Review Letters* **74** 2483

[44] Reimerdes H, Garofalo A M, Jackson G L, Okabayashi M, Strait E J, Chu M S, In Y, La Haye R J, Lanctot M J, Liu Y Q, Navratil G A, Solomon W M, Takahashi H and Groebner R J 2007 *Physical Review Letters* **98** 055001

[45] Takechi M, Matsunaga G, Aiba N, Fujita T, Ozeki T, Koide Y, Sakamoto Y, Kurita G, Isayama A, Kamada Y and JT-60 team (JT-60 team) 2007 *Physical Review Letters* **98** 055002 (pages 4)

[46] Park J K 2011 *Physics of Plasmas* **18** 110702 (pages 4)

[47] Berkery J W, Sabbagh S A, Betti R, Bell R E, Gerhardt S P, LeBlanc B P and Yuh H 2011 *Phys.*

Rev. Lett. **106** 075004

[48] Cates C, Shilov M, Mauel M E, Navratil G A, Maurer D, Mukherjee S, Nadle D, Bialek J and Boozer A 2000 *Physics of Plasmas* **7** 3133–3136

[49] Garofalo A M, Chu M S, Fredrickson E D, Gryaznevich M, Jensen T H, Johnson L C, La Haye R J, Navratil G, Okabayashi M, Scoville J T, Strait E J, Turnbull A D and DIII-D Team 2001 *Nuclear Fusion* **41** 1171

[50] Katsuro-Hopkins O, Bialek J, Maurer D and Navratil G 2007 *Nuclear Fusion* **47** 1157–1165

[51] Sabbagh S, Ahn J W, Allain J, Andre R, Balbaky A, Bastasz R, Battaglia D, Bell M, Bell R, Beiersdorfer P, Belova E, Berkery J, Betti R, Bialek J, Bigelow T, Bitter M, Boedo J, Bonoli P, Boozer A, Bortolon A, Boyle D, Brennan D, Breslau J, Buttery R, Canik J, Caravelli G, Chang C, Crocker N, Darrow D, Davis B, Delgado-Aparicio L, Diallo A, Ding S, D'Ippolito D, Domier C, Dorland W, Ethier S, Evans T, Ferron J, Finkenthal M, Foley J, Fonck R, Frazin R, Fredrickson E, Fu G, Gates D, Gerhardt S, Glasser A, Gorelenkov N, Gray T, Guo Y, Guttenfelder W, Hahm T, Harvey R, Hassanein A, Heidbrink W, Hill K, Hirooka Y, Hooper E, Hosea J, Humphreys D, Indireshkumar K, Jaeger F, Jarboe T, Jardin S, Jaworski M, Kaita R, Kallman J, Katsuro-Hopkins O, Kaye S, Kessel C, Kim J, Kolemen E, Kramer G, Krasheninnikov S, Kubota S, Kugel H, La Haye R, Lao L, LeBlanc B, Lee W, Lee K, Leuer J, Levinton F, Liang Y, Liu D, Lore J, Luhmann Jr N, Maingi R, Majeski R, Manickam J, Mansfield D, Maqueda R, Mazzucato E, McLean A, McCune D, McGeehan B, McKee G, Medley S, Meier E, Menard J, Menon M, Meyer H, Mikkelsen D, Miloshevsky G, Mueller D, Munsat T, Myra J, Nelson B, Nishino N, Nygren R, Ono M, Osborne T, Park H, Park J, Park Y, Paul S, Peebles W, Penaflor B, Perkins R, Phillips C, Pigarov A, Podesta M, Preinhaelter J, Raman R, Ren Y, Rewoldt G, Rognlien T, Ross P, Rowley C, Ruskov E, Russell D, Ruzic D, Ryan P, Schaffer M, Schuster E, Scotti F, Shaing K, Shevchenko V, Shinohara K, Sizyuk V, Skinner C, Smirnov A, Smith D, Snyder P, Solomon W, Sontag A, Soukhanovskii V, Stoltzfus-Dueck T, Stotler D, Stratton B, Stutman D, Takahashi H, Takase Y, Tamura N, Tang X, Taylor G, Taylor C, Tritz K, Tsarouhas D, Umansky M, Urban J, Untergberg E, Walker M, Wampler W, Wang W, Whaley J, White R, Wilgen J, Wilson R, Wong K, Wright J, Xia Z, Youchison D, Yu G, Yuh H, Zakharov L, Zemlyanov D, Zimmer G and Zweben S 2013 *Nuclear Fusion* **53** 104007

[52] Turnbull A D, Hanson J M, Turco F, Ferraro N M, Lanctot M J, Lao L L, Strait E J, Piovesan P and Martin P 2016 *Journal of Plasma Physics* **82** 515820301

[53] Ferron J R, Holcomb C T, Luce T C, Park J M, Politzer P A, Turco F, Heidbrink W W, Doyle E J, Hanson J M, Hyatt A W, In Y, R J La Haye, Lanctot M J, Okabayashi M, Petrie T W, Petty C C and Zeng L 2013 *Physics of Plasmas* **20** 092504

[54] Berkery J, Sabbagh S, Bell R, Gerhardt S, LeBlanc B and Menard J 2015 *Nuclear Fusion* **55** 123007

[55] Poli F, Kessel C, Chance M, Jardin S and Manickam J 2012 *Nuclear Fusion* **52** 063027

Table 1. Occurrences of β-collapse precursor modes in 26 NCS discharges.

Type	Number	Fraction
TM locking	17	29.3%
$n = 1$ RWM	28	48.3%
$n = 2$ RWM	2	3.4%
Internal kink	4	6.9%
ELM	7	12.1%
Total	**58**	

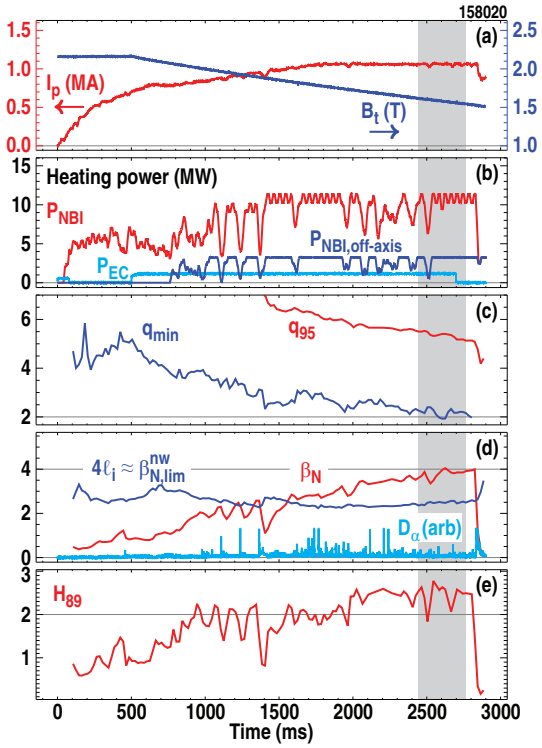

Figure 1. (Color online) Timeseries from DIII-D discharge 158020 showing (a) plasma current I_p and toroidal field B_t, (b) total NBI, off-axis NBI, and EC heating power, (c) minimum safety factor q_min and safety factor at the 95% flux surface q_{95}, (d) normalized beta, β_N, the approximate no-wall limit scaling of four times the normalized internal inductance, and deuterium-α emission intensity, and (e) L-mode confinement enhancement factor H_{89}.

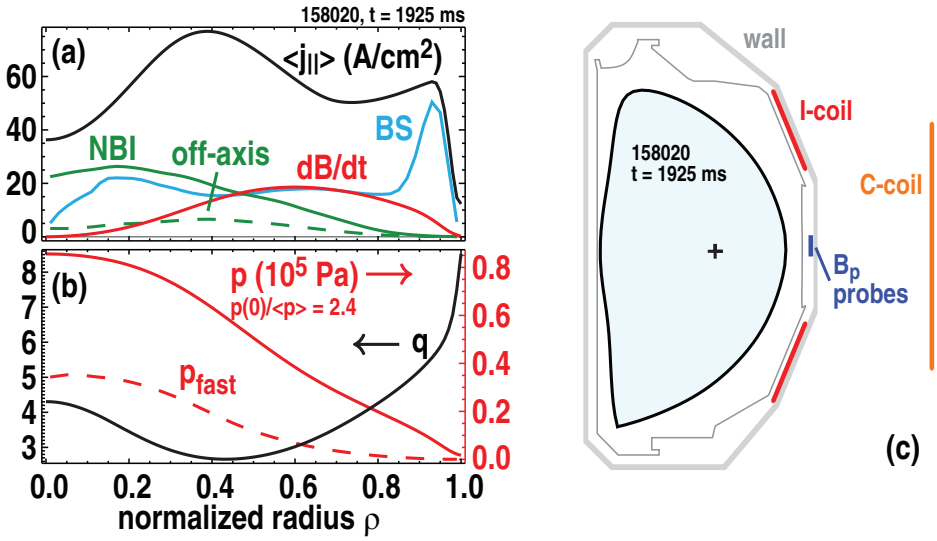

Figure 2. (Color online) Equilibrium (a) current density profile, showing contributions from total NBI, the off-axis NBI portion, toroidal field ramp induced, and bootstrap, (b) safety factor and pressure profiles, showing the total and fast ion pressure, and (c) shape for DIII-D shot 158020 at $t = 1925$ ms.

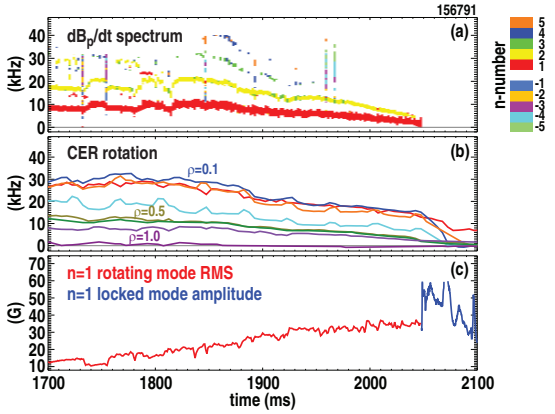

Figure 3. (Color online) Timeseries from the locking of an $(m, n) = (3, 1)$ TM showing (a) a spectral decomposition of $\mathrm{d}B_\mathrm{p}/\mathrm{d}t$ signals colored by n-number, (b) carbon impurity rotation data from CER spectroscopy channels spanning the plasma minor radius, and (c) RMS amplitude of integrated $\mathrm{d}B_\mathrm{p}/\mathrm{d}t$ fluctuation measurements (red) compared with the amplitude of the final $n = 1$ locked mode (blue).

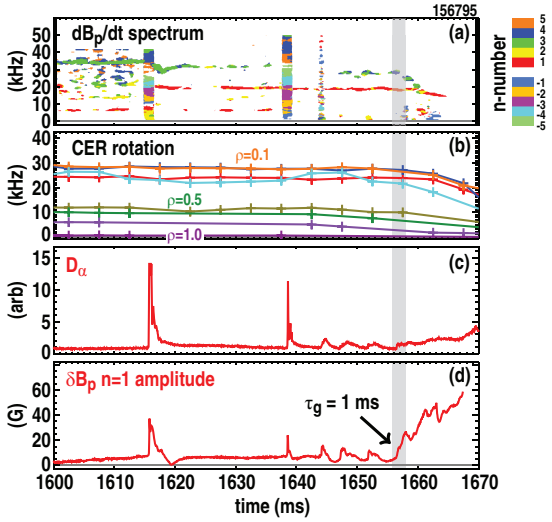

Figure 4. (Color online) Timeseries from a born-locked instability showing (a) a spectral decomposition of $\mathrm{d}B_\mathrm{p}/\mathrm{d}t$ signals colored by n-number, (b) carbon impurity rotation data from CER spectroscopy channels spanning the plasma minor radius, (c) edge D_α emission, and (d) the $n = 1$ fluctuation amplitude from integrated B_p measurements.

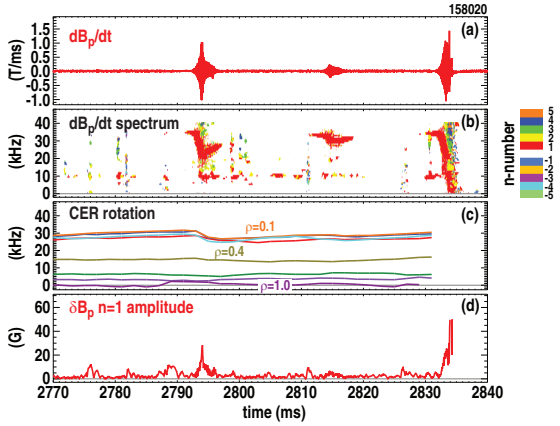

Figure 5. (Color online) Timeseries from a quickly growing and rotating internal instability showing (a) an example $\mathrm{d}B_\mathrm{p}/\mathrm{d}t$ measurement, (b) a spectral decomposition of $\mathrm{d}B_\mathrm{p}/\mathrm{d}t$ signals colored by n-number, (c) carbon impurity rotation data from charge CER spectroscopy channels spanning the plasma minor radius, and (d) the $n = 1$ fluctuation amplitude from integrated B_p measurements.

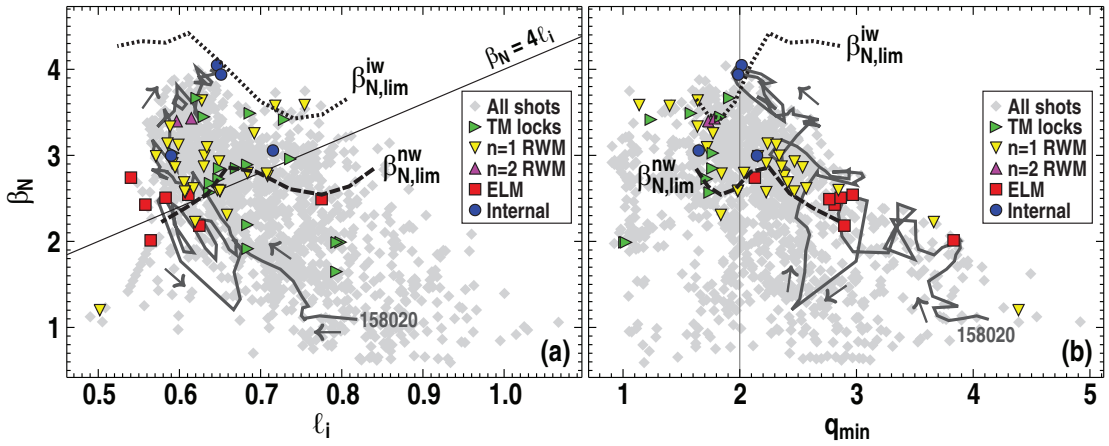

Figure 6. (Color online) 50 ms time-averages of the parameter space (lozenges) accessed by DIII-D NCS experiments in terms of (a) β_N vs ℓ_i and (b) β_N vs q_{min}, with β-collapses due to TM locking events (right-pointing triangles), and $n = 1$ and $n = 2$ RWMs (downward and upward triangles), ELMs (squares) and internal kink modes (circles), as well as no- and ideal-wall β_N-limits predicted by ideal MHD based on scaled experimental equilibria (dashed and dotted curves), and the evolution of DIII-D discharge 158020 (solid curves).

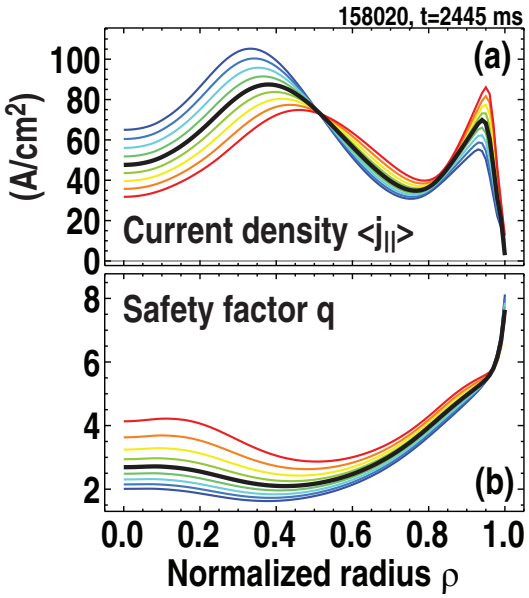

Figure 7. (Color online) Experimental (black curves) and artificially scaled (colored curves) parallel current density (a) and safety factor (b) profiles used for ideal MHD β_{N} limit calculations.

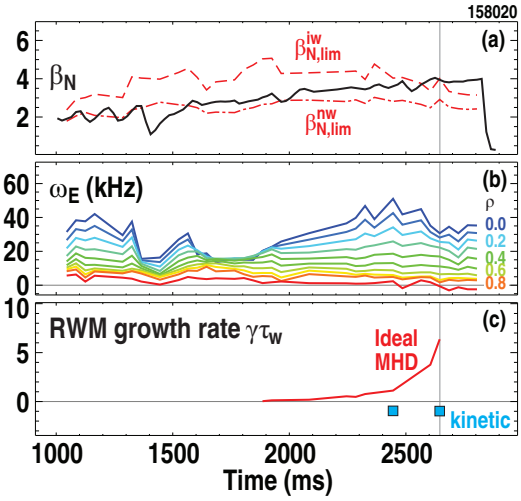

Figure 8. (Color online) Timeseries of (a) β_N (solid curve) and ideal MHD no-wall (dot-dashed) and ideal-wall (dashed) limits, (b) ω_E rotation at selected radii across the plasma cross section, and (c) the RWM growth rate predicted with (squares) and without (solid) curve kinetic contributions to the ideal MHD dispersion relation.

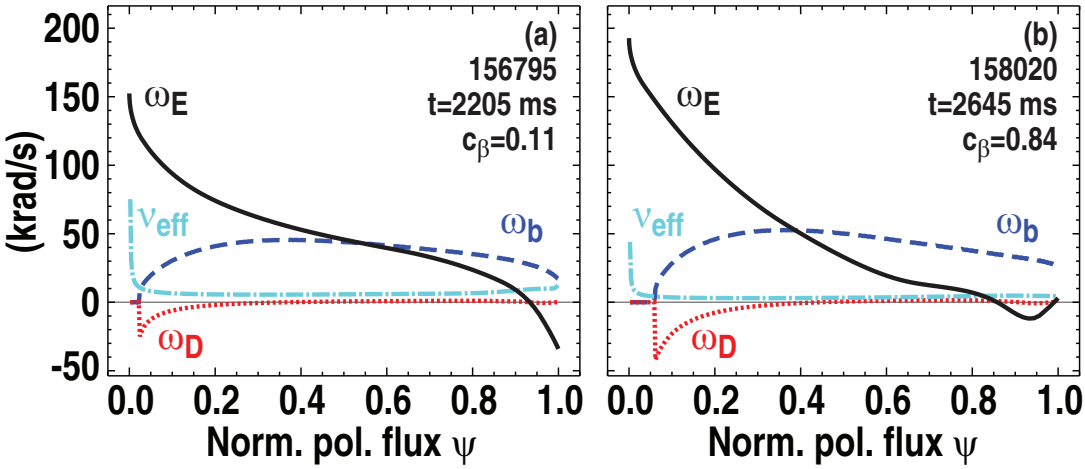

Figure 9. (Color online) Profiles of $\omega_{\rm E}$ rotation (solid curves), effective electron–ion collision frequency $\nu_{\rm eff}$ (dot-dashed), and the bounce $\omega_{\rm b}$ (dashed) and precession drift $\omega_{\rm D}$ (dotted) frequencies of trapped ions for two experimental cases.

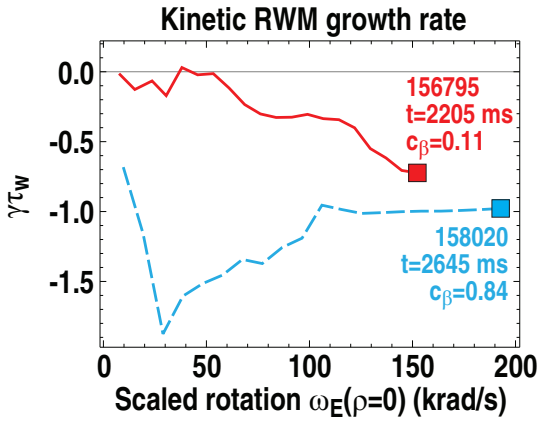

Figure 10. (Color online) RWM growth rate predicted by the kinetic dispersion relation as a function of scaled ω_E rotation at the magnetic axis for two cases. The square symbols indicate the original, experimental rotation values.

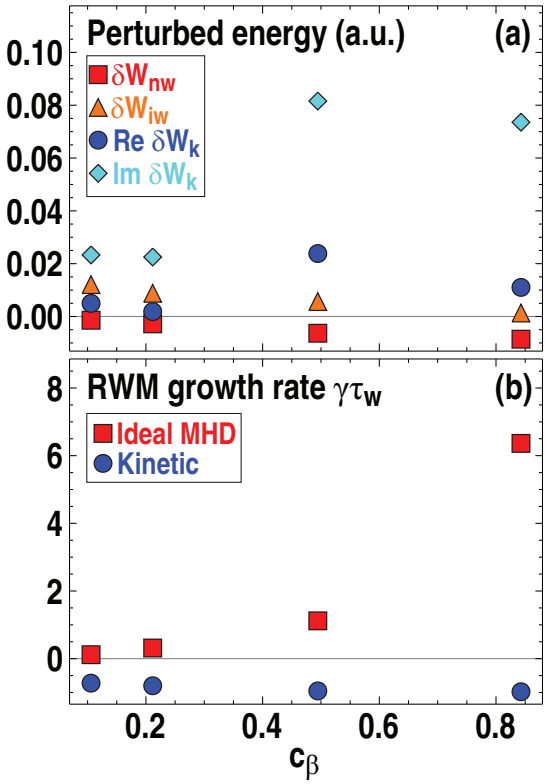

Figure 11. (Color online) Dependence on the normalized distance c_β between the no-wall and ideal-wall β_N limits of (a) ideal MHD no-wall (squares), ideal MHD ideal-wall (triangles), and real and imaginary kinetic (circles and lozenges) perturbed potential energies; and (b) RWM growth rates from the ideal MHD only (squares) and kinetic (circles) dispersion relations. The two lower c_β cases are from DIII-D discharge 156795 at $t = 2205$ and 2245 ms, and the two higher c_β cases are from discharge 158020 at $t = 2445$ and 2645 ms.

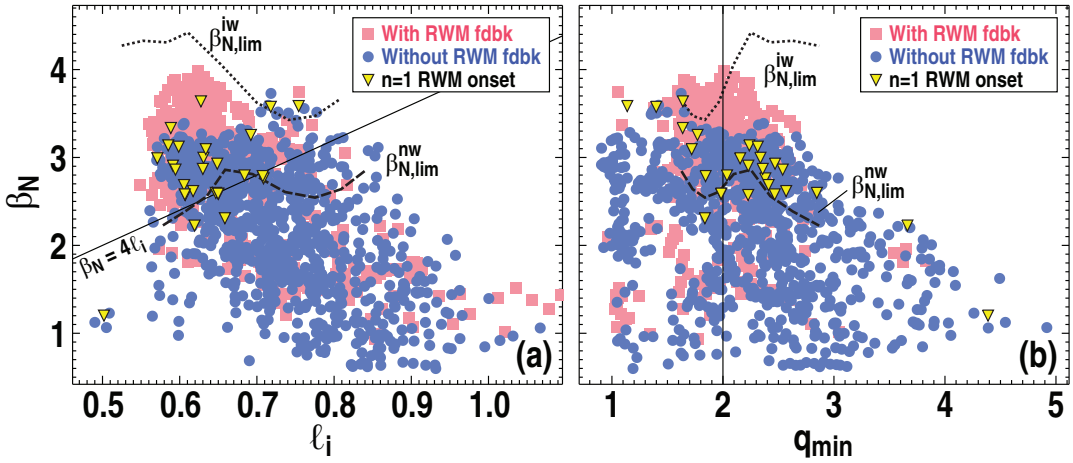

Figure 12. (Color online) 50 ms time-averages of experimentally accessed (a) β_N vs ℓ_i and (b) β_N vs q_{min} values, with (squares) and without (circles) RWM feedback control, β-collapses due to $n = 1$ RWM events (triangles), and no-wall (dashed curve) and ideal-wall (dotted curve) ideal MHD β_N limits obtained from scaled experimental equilibria.